Supporting Information

Electrochemical acid-base generators for decoupled carbon management

Dawei Xi[1,3] *, Zheng Yang[1,3], Michael Emanuel[1], Panlin Zhao[1], Michael J. Aziz[1] *

1 Harvard John A. Paulson School of Engineering and Applied Sciences, Cambridge, MA, USA.

3 These authors contributed equally: Dawei Xi and Zheng Yang

* E-mail: daweixi@fas.harvard.edu; maziz@harvard.edu

Table of Contents

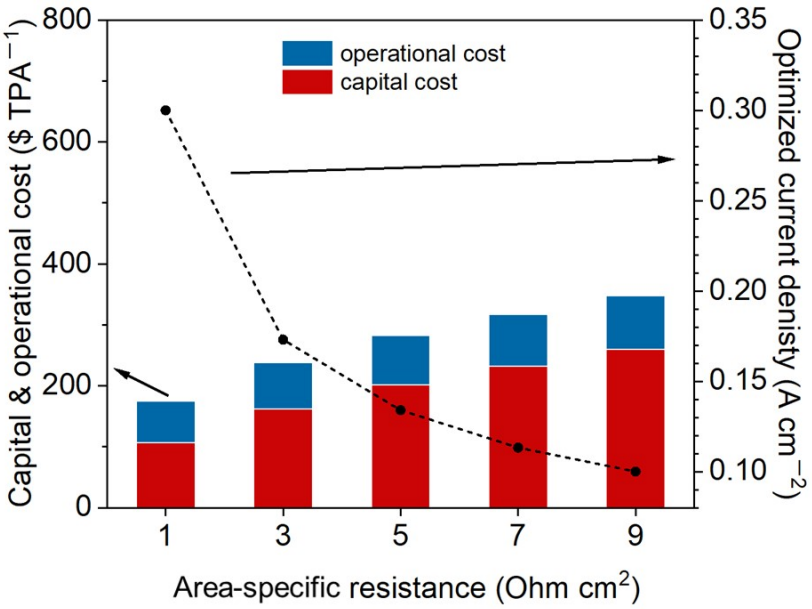

Supplementary Fig. S1 | Increased capital cost and operational cost with higher area-specific resistance.

The capital cost and operational cost increase with a higher area-specific resistance. With the current density optimized to maximize the net product value (NPV), a higher area-specific resistance will decrease the suitable current density. With the same production amount required, higher cell area and facilities are required, leading to a higher capital cost. The operational cost also increases due to the higher voltage required under suitable operation conditions. Detailed technoeconomic models used for the calculation are described in Supplementary Fig. S21.

Supplementary Table S1: Comparison between electrochemical acid-base generators

Important parameters like current density, energy cost, current efficiency of CO_2 capture, CO_2 source concentration, CO_2 outgas concentration and dead volume are correlated, if these processes are not decoupled. Only achieving a few good numbers at one specific operation condition is not very helpful. Only when all of the parameters are optimized during the cycled or steady-state operation, can an electrochemical cell be potentially practical.

Method	Energy consumption (kJ/mol charge)	Current efficiency (%)	Note
Solid-electrolyte reactor, CEM-AEM (O_2 looping)[1]	140 (200 mA cm^{-2}) 220 (200 mA cm^{-2})	~ 80% (6000 ppm CO_2, current density 20 mA cm^{-2}) ~ 40 (400 ppm CO_2, current density 3 mA cm^{-2})	Coupled oxygen reduction (base generation) and CO_2 capture. CO_2 absorption reaction kinetic limits the current density and efficiency.
Solid-electrolyte reactor, CEM-CEM (H_2 looping)[2]	95 (20 mA cm^{-2}) 207 (200 mA cm^{-2})	90% – 98%	CO_2 outgas in the center chamber. Bubble formation in the center can interfere with performance if scaled up.
Salt splitting, CEM-AEM (water splitting)[3, 4]	> 240 (20 mA cm^{-2}) > 350 (200 mA cm^{-2})	~65% (for 1 M acid-base production)	Energy consuming. Low efficiency.
Alternating electrolysis (H_2 looping, I_2 mediating)[5]	140 (100 mA cm^{-2})	Not available	Requiring Li, iodide, and alternative electrolysis management.
BPM salt splitting, CEM-BPM-CEM (ferro-ferricyanide looping)[6]	> 150 (50 mA cm^{-2}) > 200 (10 mA cm^{-2})	~70%	High resistance, low current density, high energy cost, bubble formation in the center chamber.
Salt splitting, AEM-CEM (H_2 looping)[7]	~ 100 (10 mA cm^{-2})	Not available	Strong acid formation, current efficiency limited.
CEM-CEM (H_2 looping)[8, 9]	> 100 (10 mA cm^{-2})	> 90%	High resistance, Low current density, high energy cost, bubble formation in the center

			chamber.
Salt splitting, AEM-CEM (water splitting)[10]	~250 (6 mA cm^{-2})	Not available	Green $Ca(OH)_2$. high resistance, Low current density, high energy cost, solid formation in the cell.
GDE-AEM-GDE (H_2 looping)[11]	~140 (10 mA cm^{-2}) ~180 (20 mA cm^{-2})	~ 50%	High resistance, bubble formation in the center.
This work	100 (20 mA cm^{-2}) 240 (200 mA cm^{-2})	> 94%	Decoupled acid-base generation with relatively lower energy cost. Adjustable accumulated concentration of the generated acid-base. Suitable for carbon capture, green $Ca(OH)_2$ production. Compatible with fluctuating sources.

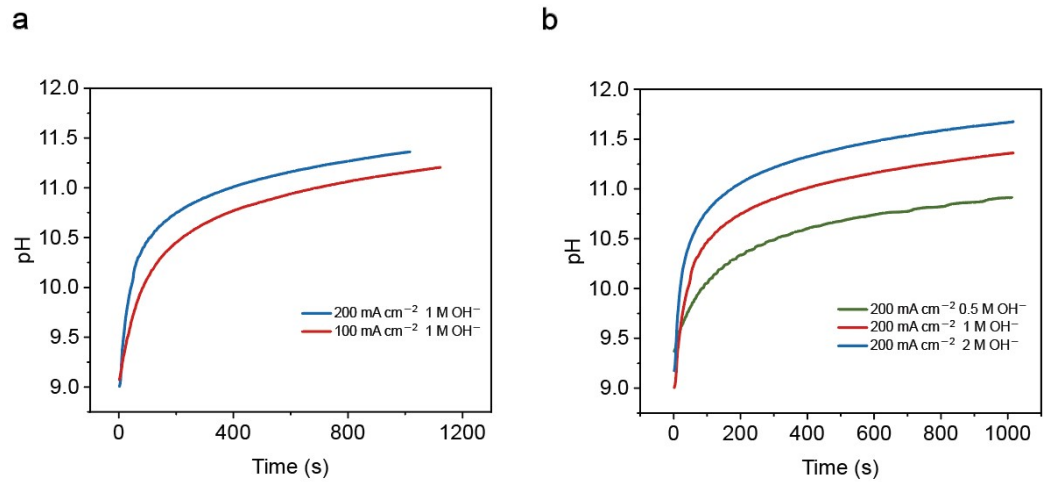

Supplementary Fig. S2 | In-situ pH change of the anolyte during hydroxide ion crossover test. a, pH changes in the anode side under different current densities when 1 M NaOH in the cathode. **b,** pH changes in the anode side under different concentrations of NaOH in the cathode side when applying a current density of 200 mA cm^{-2}.

The pH of the anolyte, running a non-proton-coupled oxidation reaction, was adjusted to approximately 7 at the beginning of the test, functioning as the hydroxide ion crossover acceptor side. We set six experiments (Exp 1 – 6) to figure out the impact of the concentration of hydroxide ions and current density on hydroxide ion crossover. Conditions used in each experiment are listed in **Supplementary Table. S2**.

Supplementary Table. S2 | Experimental conditions used for hydroxide ion crossover tests.

	Exp 1	Exp 2	Exp 3	Exp 4	Exp 5	Exp 6
Current density (mA cm^{-2})	200	200	200	100	100	100
Concentration of NaOH in the catholyte (mol L^{-1})	0.5	1	2	0.5	1	2

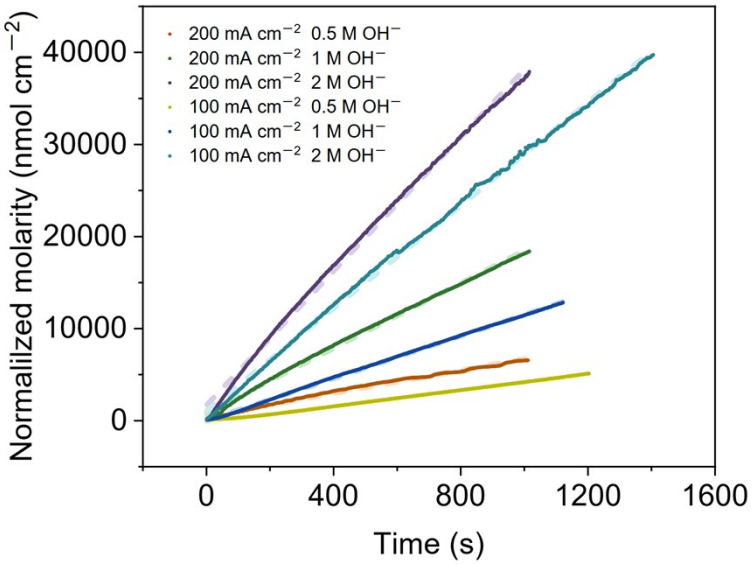

Supplementary Fig. S3 | Area normalized molarity of hydroxide ions in the anolyte (acceptor side) over time during hydroxide ion crossover test. Dashed lines are the linear fitting curves of the corresponding molarity data.

Because pH equals $-log[H^+]$, we calculate the concentration of protons as 10^{-pH}. The concentration of OH^- can be calculate as 10^{14-pH}. The amount of OH^- in the solution is $V * 10^{14-pH}$. V is the volume of the anolyte. Then the amount of OH^- is normalized by the cell area. Supplementary Fig. S3 is derived accordingly using data in Supplementary Fig. S2. Through linear fitting, we calculated the slope of normalized amount of OH^- for each experiment. The crossover flux is the slope of the line. The linear fitting functions are listed in **Supplementary Table. S3**.

Supplementary Table. S3 | Linear fitting results for hydroxide ion crossover tests.

Parameters (current density/concentration of hydroxide ion in the cathode side)	Function	R^2
200 mA cm^{-2}/ 0.5 mol L^{-1}	$y = 6.219x + 495.9$	0.99167
200 mA cm^{-2}/ 1 mol L^{-1}	$y = 17.64x + 814.0$	0.99703
200 mA cm^{-2}/ 2 mol L^{-1}	$y = 36.44x + 1675$	0.99715
100 mA cm^{-2}/ 0.5 mol L^{-1}	$y = 4.332x - 160.2$	0.99902
100 mA cm^{-2}/ 1 mol L^{-1}	$y = 11.52x - 14.27$	0.99961
100 mA cm^{-2}/ 2 mol L^{-1}	$y = 27.94x + 1037$	0.99865

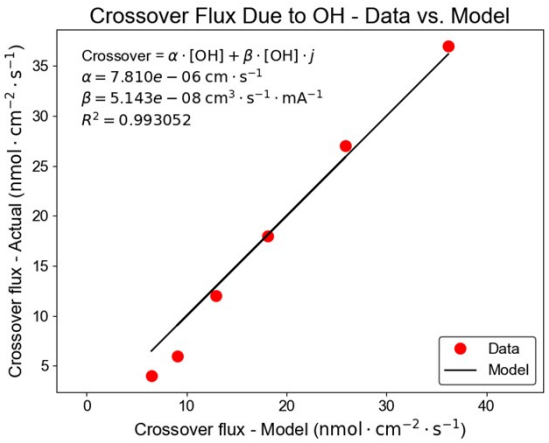

Supplementary Fig. S4 | Fitting of hydroxide ion crossover experimental data.

Then, the crossover flux under various experimental conditions are fitted using a two factor model, with coefficients for diffusion and electromigration, according to Nerst-Planck equation.

The function used for fitting is **Equation S1**. In which, $c(OH^-)$ is the concentration of hydroxide ion in the catholyte (source) during crossover test. j is the current density applied through the cell.

$$Crossover\ flux = \alpha * c(OH^-) + \beta * c(OH^-) * j \quad \text{(S1)}$$

The resulting α, β and R^2 are listed in the figure.

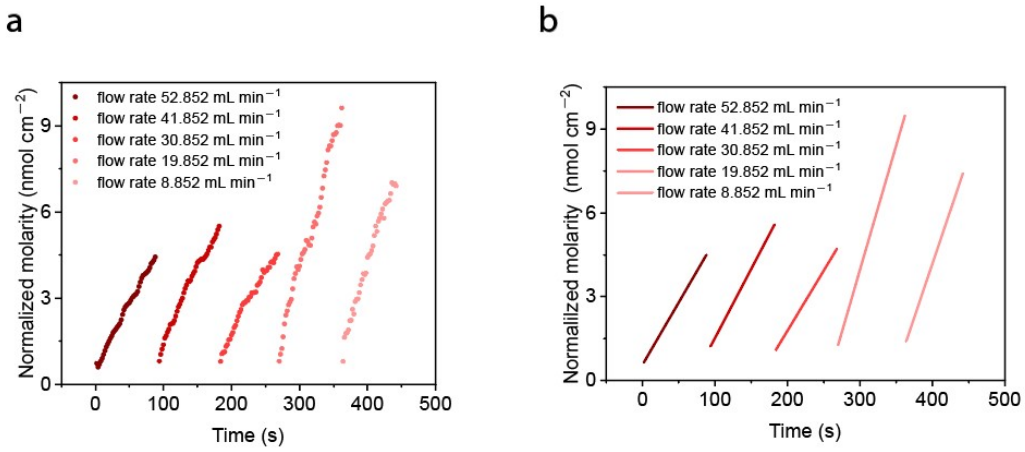

Supplementary Fig. S5 | Area normalized molarity of protons in the catholyte (acceptor side) over time during proton crossover test with various center flow rates. The current density used for the tests is 200 mA cm^{-2} with 2 M NaOAc cycled in the center chamber. **a,** Experimental data of area normalized molarity of protons in the catholyte (acceptor side) over time. **b,** Linear fitting curves of the corresponding experimental data.

The pH of the catholyte, running a non-proton-coupled reduction reaction, was adjusted to approximately 7 at the beginning of the test, functioning as the proton crossover acceptor side. The calculation and normalization is similar to the method described in Supplementary Fig. S3. The linear fitting functions are listed in **Supplementary Table. S4**.

Supplementary Table. S4 | Linear fitting results for proton crossover tests with various center flow rates.

Flow rate (mL min^{-1})	Function	R^2
52.852	$y = 0.04458x + 0.57093$	0.99542
41.852	$y = 0.04943x - 3.41741$	0.99247
30.852	$y = 0.04301x - 6.82107$	0.98268
19.852	$y = 0.08912x - 22.77862$	0.98476
8.852	$y = 0.07687x - 26.57269$	0.98757

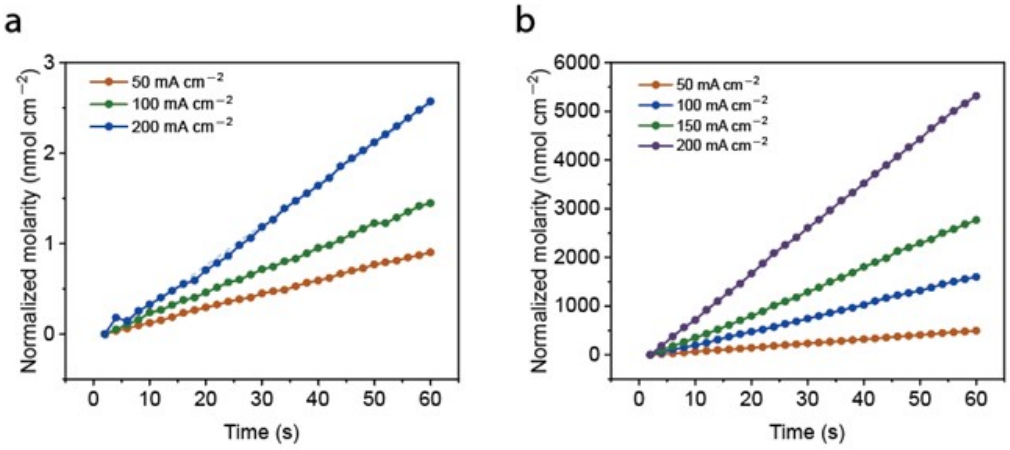

Supplementary Fig. S6 | Area normalized molarity of protons in the catholyte (acceptor side) over time during proton crossover test with various current densities and center chamber electrolytes during proton crossover test. a, Experimental data of area normalized molarity of protons in the catholyte (acceptor side) over time, with 2 M NaOAc cycled in the center chamber. **b,** Experimental data of area normalized molarity of protons in the catholyte (acceptor side) over time, with 1 M NaOAc adding 1 M HOAc cycled in the center chamber. The tests are done using various current densities as labeled in the figures. Dashed lines are the linear fitting curves of the corresponding normalized molarity data.

The pH of the catholyte, running a non-proton-coupled reduction reaction, was adjusted to approximately 7 at the beginning of the test, functioning as the proton crossover acceptor side. The calculation and normalization is similar to the method described in Supplementary Fig. S3. The linear fitting functions are listed in **Supplementary Table. S5 – S6**.

Supplementary Table. S5 | Linear fitting results for proton crossover tests with various current densities with 2 M NaOAc cycled in the center chamber.

Current density (mA cm^{-2})	Function	R^2
50	$y = 0.01562x - 0.02657$	0.99915
100	$y = 0.02469x - 0.03479$	0.99908
200	$y = 0.04479x - 0.13987$	0.99713

Supplementary Table. S6 | Linear fitting results for proton crossover tests with various current densities with 1 M NaOAc and 1 M HOAc cycled in the center chamber.

Current density (mA cm^{-2})	Function	R^2
50	$y = 8.6417x - 24.58814$	0.99964

100	$y = 28.01025x - 81.32755$	0.99925
150	$y = 48.46496x - 143.1881$	0.99924
200	$y = 92.43337x - 179.3562$	0.99986

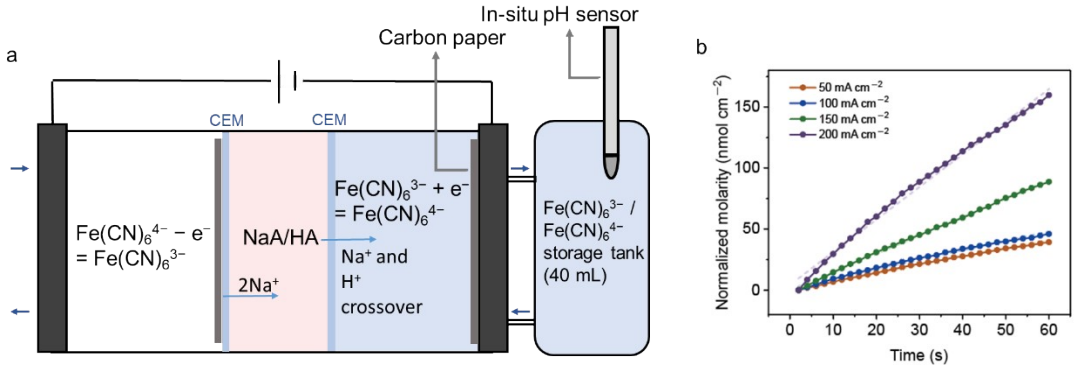

Supplementary Fig. S7 | Proton crossover test without external proton sources. **a,** Schematic of a three-chamber two-membrane cell used for proton crossover test, without proton sources from the anolyte. **b,** Area normalized molarity of protons in the catholyte (acceptor side) over time during proton crossover test with various current densities. 1 M NaOAc adding 1 M HOAc was cycled in the center chamber.

In the test where no protons were generated and transported from the anolyte, 40 mL 0.4 M $K_4Fe(CN)_6$ was cycled though anode chamber, using three pieces of baked carbon papers as electrodes, with other conditions identical to the previous proton crossover tests. The proton crossover in this case can only come from the center chamber acetic acid. The pH of the catholyte, running a non-proton-coupled reduction reaction, was adjusted to approximately 7 at the beginning of the test, functioning as the proton crossover acceptor side. The calculation and normalization is similar to the method described in Supplementary Fig. S3. The linear fitting functions are listed in **Supplementary Table. S7**.

Supplementary Table. S7 | Linear fitting results for proton crossover tests without external proton sources. The tests are done with various current densities with 1 M NaOAc adding 1 M HOAc cycled in the center chamber, without proton sources from the anolyte.

Current density (mA cm^{-2})	Function	R^2
50	$y = 0.67401x + 0.32575$	0.99564
100	$y = 0.77193x - 1.71506$	0.98986
150	$y = 1.50968x - 0.52912$	0.99872
200	$y = 2.67053x + 4.3645$	0.99331

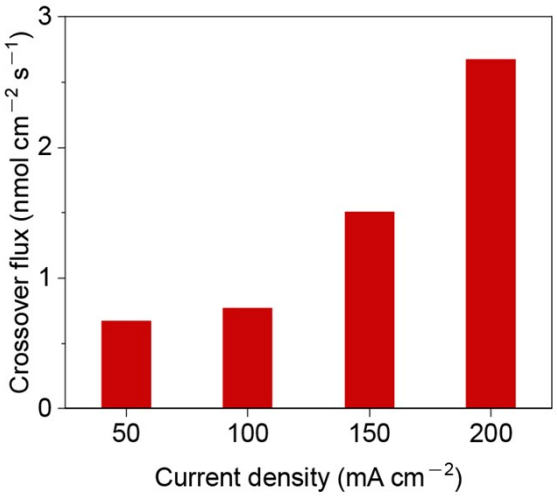

Supplementary Fig. S8 | Proton crossover fluxes without external proton sources.

The tests are done with various current densities, with 1 M NaOAc adding 1 M HOAc cycled in the center chamber. Ferrocyanide oxidation was used for anolyte, functioning as a non-proton-coupled reduction reaction and donating only sodium ions into the center chamber.

Under the same current density, the obtained crossover fluxes are much lower than the ones with proton sources from the anolyte using 1 M NaOAc adding 1 M HOAc cycled in the center chamber. The obtained crossover fluxes are slightly higher than the ones with proton sources from the anolyte using 2 M NaOAc cycled in the center chamber. This indicates that, with HOAc accumulating in the center chamber, the increasing proton crossover is due to the decreased buffer strength of 1 M NaOAc and 1 M HOAc compared to 2 M NaOAc, causing protons directly crossing two membranes. A small portion of crossover of protons are due to the ionization of HOAc and HOAc crossover as a whole molecule.

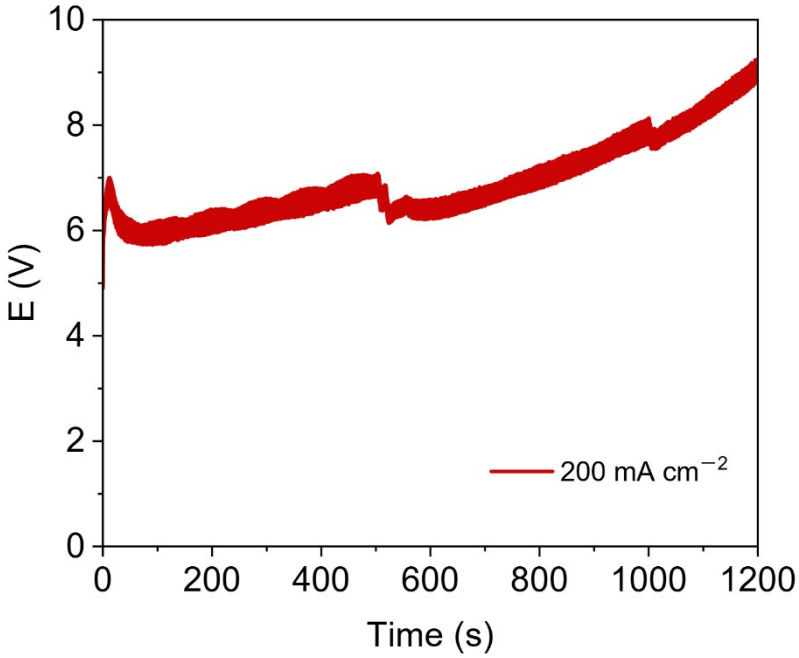

Supplementary Fig. S9 | E-t curve during operation under 200 mA cm^{-2} when using sodium polyacrylic acid (NaPAA, MW ~ 2000) in the center chamber as electrolyte.

Polyacrylic acid (PAA) is a polymeric weak acid, the conductivity of NaPAA is lower than NaOAc. During the cell operation, the cell voltage is higher than the cell using NaOAc. The large, ionized polymer chain, however, can prohibit the crossover of PAA anions or acids. Adding extra supporting salts (e.g., NaCl) can help lower the resistance of the cell. This strategy can also be applied to the NaOAc cell to decrease the resistance of the cell during operation, especially when accumulating HOAc and decreasing NaOAc dramatically increasing the cell resistance and the center chamber ionic ohmic resistance.

Supplementary Note. S1 | Numerical methods of the simulation of the distribution of H^+, Na^+, and HOAc in the center chamber

The experimental system was modeled in two dimensions by unfurling the serpentine flow field into one dimension along the flow direction (x). The second dimension in the simulation (y) is normal to the plane of the flow field. The third spatial dimension is implicitly treated as being uniform and not included directly in the calculations. This idealization is justified because the thickness of the center chamber (0.1 cm) is significantly less than the width of the channels in the flow field (11.2 cm).

The physical phenomena modeled included advection, diffusion, electromigration and chemical equilibrium. The three mass transport phenomena (advection, diffusion and electromigration) were described by the Nernst-Planck equation (Equation. S2).

$$\frac{\partial c_j}{\partial t} = -u \cdot \nabla c_j + D_j \nabla^2 c_j + \frac{z_j D_j F}{RT} \nabla \cdot (c_j \nabla \phi) \tag{S2}$$

where c_j is the concentration (mM), t is time (s), u is the fluid velocity vector (m/s), D_j the diffusivity (m^2/s), z_j the dimensionless charge number, and φ the potential (volts). Parameters named with suffix j correspond to the j-th species. The five species under consideration in this simulation are H^+, Na^+, HOAc, OAc^-, and OH^-. F is Faraday's constant; R is the ideal gas constant and T is the temperature in Kelvin. Units for concentration in the simulation are in millimolar because this corresponds to moles per cubic meter and is therefore consistent with the selected SI units for all the other quantities in the simulation.

The fluid velocity u was solved analytically by treating the system as a plane Poiseuille flow with a known volumetric flow rate. The simulation assumes a uniform electric field oriented along the y axis between the anode and cathode; the applied voltage difference is a simulation input. A diffusivity of $9.30*10^{-5}$ cm^2/s was used for H^+ and OH^-. A diffusivity of $1.11*10^{-5}$ $cm^2\ s^{-1}$ was used for HOAc and OAc^-. The diffusivity of Na^+ was $1.33*10^{-5}$ $cm^2\ s^{-1}$. The operating temperature was taken as 25 °C. The applied potential was selected so the output current density match the experimentally observed current density of 200 mA cm^{-2}.

The simulation domain was divided into a grid of 256*64 rectangular cells with dimensions 0.044*0.0016 cm in the x and y dimensions, respectively. The advection operator was calculated with a first order finite difference with upwinding, i.e. the concentration gradient was taken comparing a cell to its left-hand neighbor because the flow is from left to right. The diffusion operator was calculated with the standard centered finite difference comparing a cell to its four neighbors. Since we assumed a constant electric field E_0, the electromigration term significantly simplifies and only depends on the gradient of the concentration along the y axis multiplied by known scalars. This gradient was calculated analogously to the x gradient used for advection.

The boundary conditions at the inlet (column where x = 0) are the known concentrations of each species arising from a 2.0 M solution of NaOAc. The bottom of the simulation (y = 0) corresponds to the row of cells next to the anodic CEM. All current in these cells is treated as being due to H^+ entering through the CEM. It is not necessary to impose a boundary condition at the top, corresponding to the cathodic CEM, because the electric field is pushing mainly Na^+ with a small amount of H^+ through the CEM.

One time step of the simulation begins with application of the discretized advection, diffusion, and electromigration operators, respectively, to all five species under consideration. A small correction is then made to impose electroneutrality, which would not otherwise hold exactly. The preliminary concentrations of the five species will typically not be in chemical equilibrium. We consider two chemical equilibria to apply: acid dissociation for acetic acid, with a pK_a of 4.76; and the water dissociation equilibrium. These two equilibrium conditions are imposed in order, by solving a simple quadratic equation. The physical rationale is that these are fast chemical equilibria that are achieved at time scales significantly smaller than each time step in this simulation (which are on the order of 0.1 milliseconds). At each time step, the root mean square change in concentration is calculated. Time steps are repeated until the RMS concentration drops below a small threshold indicating that the simulation has converged to a steady state.

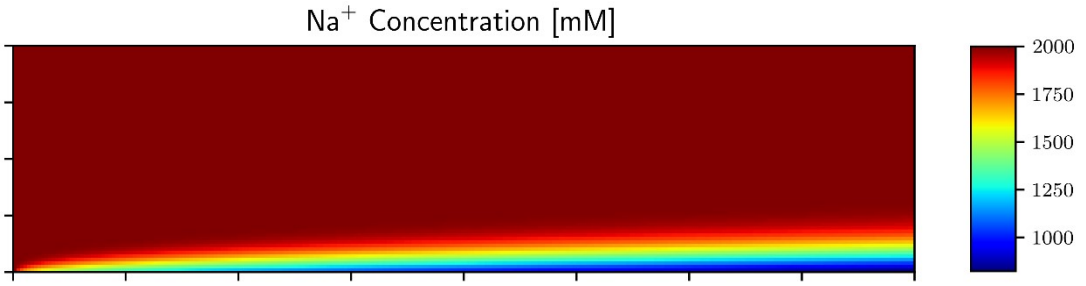

Supplementary Fig. S10 | Simulation of the distribution of Na^+ in the center chamber. The length (x axis, same as the direction of the center flow) is 11.18 cm. The height (z axis, representing the thickness of the center chamber) is 0.10 cm. The width (y axis, not shown, representing the width of the flow channels) is 0.4472 cm. The geometric area of the flow field is = 5.00 cm^2. The length is 25x longer than the width, reflecting a serpentine flow path with 5 "zig zags" in the flow field. The conditions for this simulation are: 2 M NaOAc cycled through the center chamber, at a flow rate of 30 mL min^{-1}.

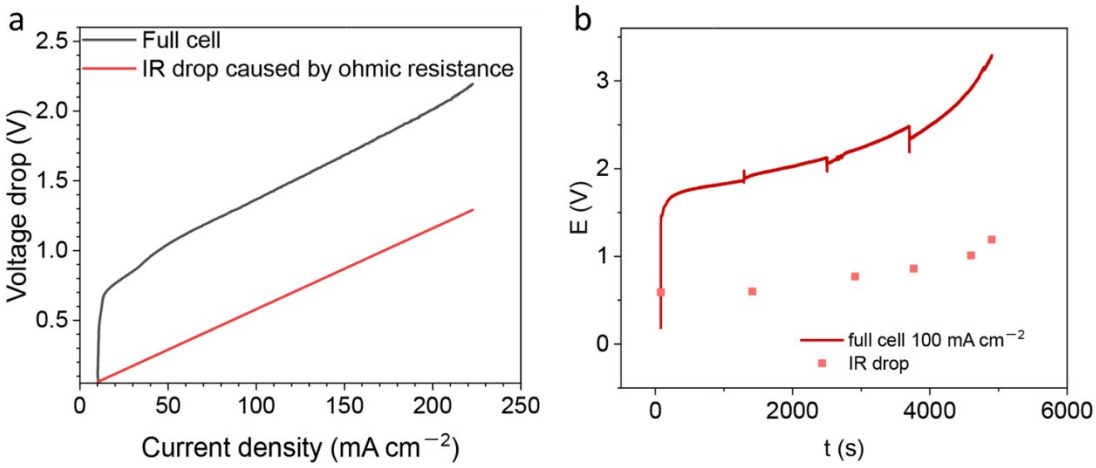

Supplementary Fig. S11 | Voltage drop from Ohmic resistance loss. a, LSV of the full cell plotted together with the calculated IR drop. **b,** Full cell V-t curve plotted together with calculated IR drop.

The major contributor to the voltage cost is ohmic resistance loss. Another contributor is ionic polarization resistance, which is more obvious under a high current density at steady state. The thermodynamic voltage required to generate a locally high concentration of (1 M) protons and (1 M) hydroxides is approximately 0.83 V. The charge transfer kinetics of the hydrogen oxidation reaction (HOR) on Pt gas diffusion electrodes (GDEs) and the hydrogen evolution reaction (HER) on PtRu are fast. Mass transport does not significantly increase the cell voltage when the current density is below 300 mA/cm^2.

The conductivity of HOAc is lower than the conductivity of NaOAc. When the proportion of HOAc increases, the high frequency resistance significantly increases, indicating that the ohmic resistance of the cell increases. Adding extra supporting salts (e.g., NaCl) can help lower the resistance of the cell under such situations to further lower the energy cost of acid-base generation.

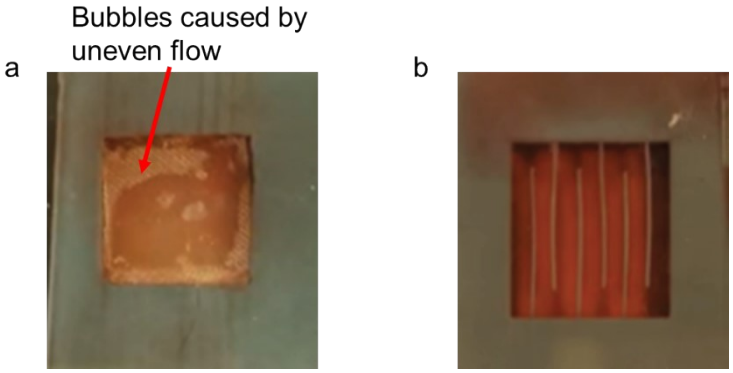

Supplementary Fig. S12 | Comparison of center chambers with and without a flow field. a, Center chamber without a flow field. **b,** Center chamber with a flow field. Red dye solution was used for visual calarification.

To figure out the impact of flow field, we sandwiched two center chmabers with two PDMS boards, and compressed with two pieces of glass. Then we used a syringe to inject dye solution into the chamber to see the flow inside the window. When there is no flow field in the center chamber, some area in the window was filled with bubble and have no solution flowed through. This "dead region" may cause the accumulation of solution, a higher local concentration of HOAc and H^+ and a higher local resistance, thus leading to higher crossover of protons. With a serpentine flow field implemented in the center chamber, the solution could be directed through the chanels and fully filled the whole window, avoiding any "dead region".

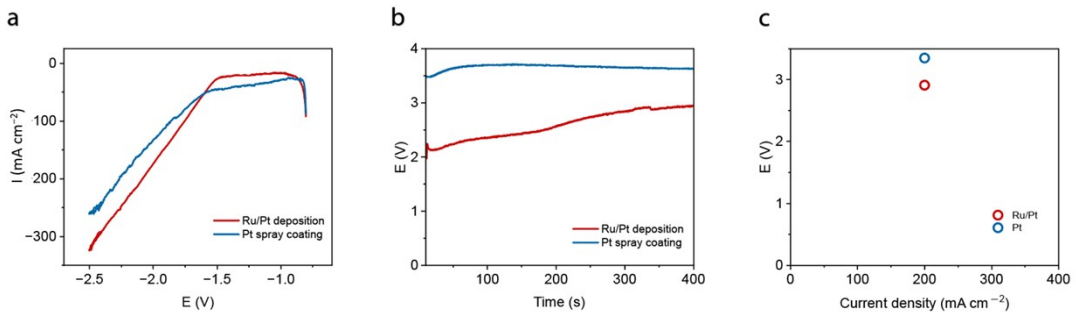

Supplementary Fig. S13 | Comparison of different HER catalysts. a, Comparison of the LSV curves using Pt and Ru/Pt. The solution used for scanning was 1 M NaOH. **b,** Comparison of E-t curve during operation. **c,** Comparison of cell voltage during the experiment.

We did LSV test in 1 M NaOH to compare the overpotential of Ru/Pt catalyst and Pt/C catalyst in hydrogen evolution reaction. Supplementary Fig. S13a shows that the overpotential of the Ru/Pt is lower than that of the Pt/C. This difference resulted in a lower operation voltage when applying Ru/Pt as cathode in the acid base generator[12] (Supplementary Fig. S13b and Fig.S13c).

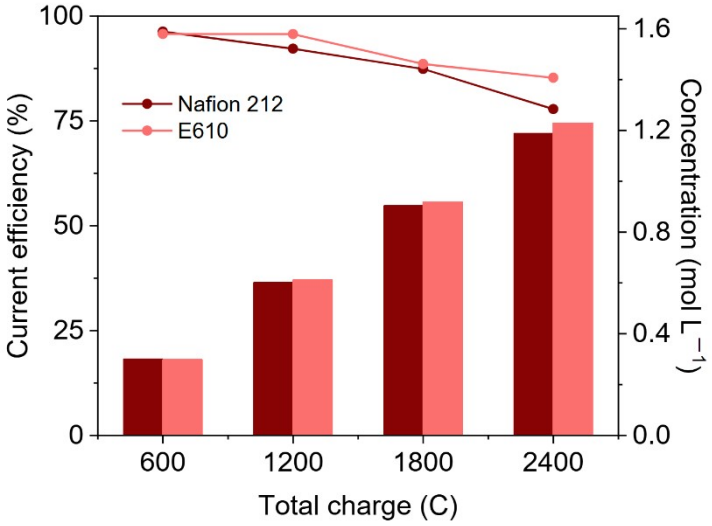

Supplementary Fig. S14 | Comparison of differential current efficiency and concentration of generated acid and base when using different membranes. Horizontal axis is the total charge passing through the circuit. Differential current efficiency is calculated by dividing the molarity of generated acid and base by the molarity of charge passing through the circuit in a short amount of time. Concentration is the accumulated concentration of generated acid and base.

We respectively used Nafion 212 and Fumasep E610 respectively in two electrochemical cells as the cation exchange membrane used between the center chamber and the cathode chamber. The membrane at this position will affect the crossover of protons. We tested the differential current efficiency and concentration of generated acid and base in the two cells. Supplementary Fig. S14 shows that the cell using E610 had a slightly higher differential current efficiency and concentration of NaOH. This phenomenon can be explained by the higher proton transport rate in Nafion 212.

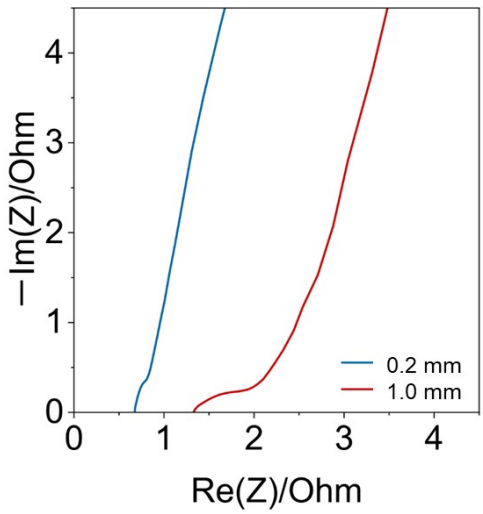

Supplementary Fig. S15 | Comparison of Nyquist plot when using center chambers with different thickness.

By changing the thickness of the center chamber in the 3D model, we can obtain center chambers with different thickness. We used one center chamber with a thickness of 0.2 mm and another one with 1.0 mm to assemble the 5 cm^2 electrochemical cell. The Nyquist plot (Supplementary Fig. S15) shows that the high frequency resistance of the cell with the thinner center chamber was almost half of the resistance of the cell with the thicker center chamber. The cell voltage was reduced, leading to a lower electricity cost.

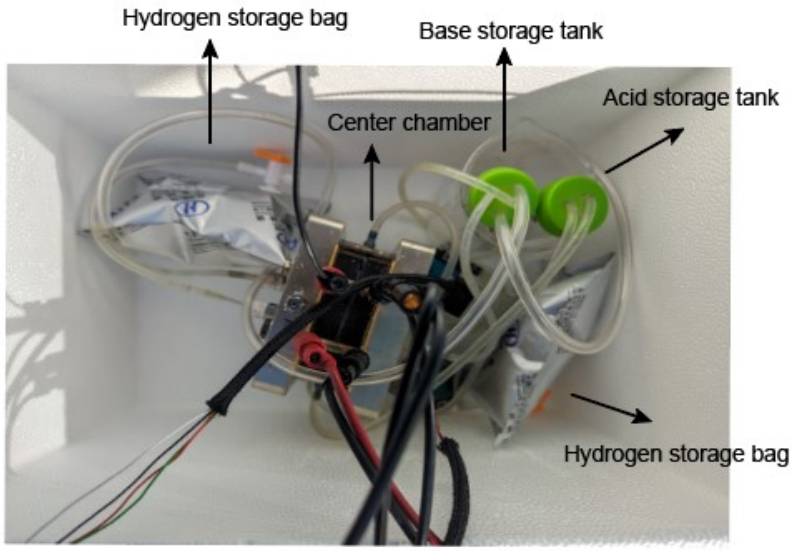

Supplementary Fig. S16 | Digital photo of the acid-base generator powered by solar energy with H_2 looping in the cell.

Here we used two hydrogen storage bags to realize looped hydrogen in the cell. Initially, H_2 was pushed through the cell to remove the remaining air in the cell. After the removal process was done, a gas bag was filled with H_2 in advance. This gas bag was connected to the anode chamber. Then the outlet of the gas bag was immediately closed, with only H_2 gas in the cell system to initiate the reaction. Hydrogen was cycled in this closed system but was not pumped or flowed in the system.

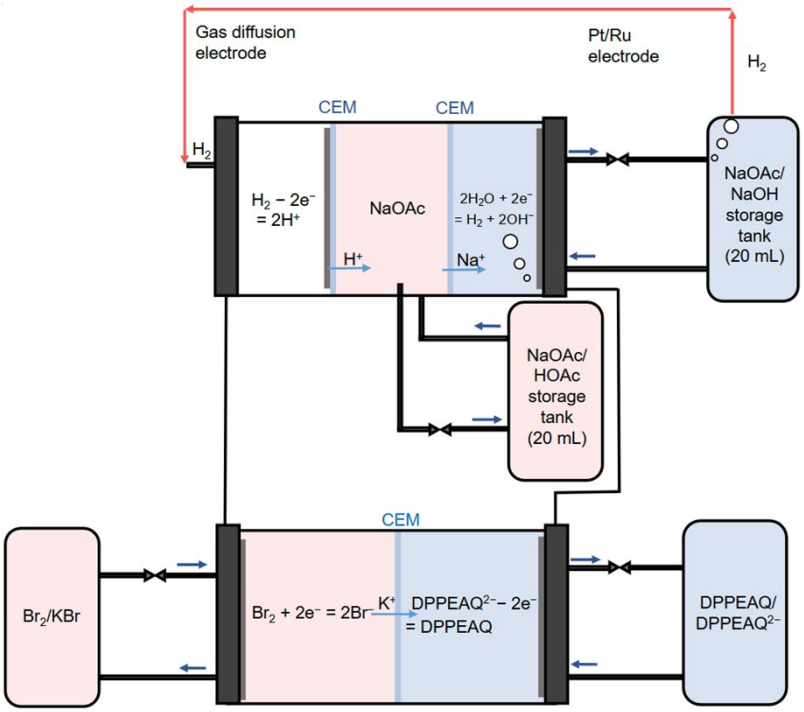

Supplementary Fig. S17 | Schematic of the acid-base generator powered by flow battery.

To power the generator by flow batteries[13], the cathode and anode were connected to a 2.5 cm^2 flow battery using three pieces of baked SGL-39AA as electrodes for each side. 40 mL 1 M pH 4 KBr was used as the posolyte and 40 mL pH 12 0.2 M DPPEAQ supported by 1 M NaCl was used as negolyte (capacity limiting side). The flow battery was first charged under constant current of 40 mA cm^{-2} to 90% state of charge. Then the Br_2 side was connected to the anode of the generator and the DPPEAQ side was connected to the cathode of the generator. Two multimeters were immediately connected to the generator to measure the voltage and current. After the current decreased below 0.01 A, we disconnected the flow battery and the generator.

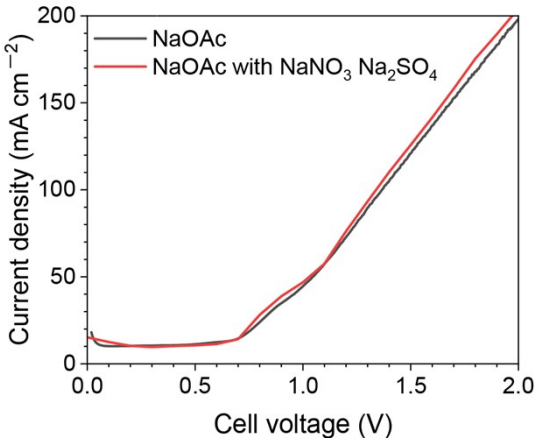

Supplementary Fig. S18 | Polarization of the electrochemical cell with potential contamination salts in the cell using LSV.

The presence of NO_x and SO_x in flue gas is a well-known challenge for conventional CO_2 capture methods, as these species degrade amines and porous sorbents over time. In contrast, our electrochemically driven acid-base generator operates in a fundamentally different manner, wherein the generated acid and base are utilized outside the electrochemical cell. Consequently, NO_x and SO_x do not interact directly with the catalysts responsible for the hydrogen evolution reaction (HER) or the hydrogen oxidation reaction (HOR), so there is no concern of catalyst deactivation. However, the introduction of SO_x and NO_x into the system leads to two primary consequences: (1) net consumption of the generated base, and (2) the formation of salts such as Na_2SO_3, Na_2SO_4, and $NaNO_3$ in the center chamber electrolyte.

To assess the effect of these species on system performance, we conducted polarization measurements with 0.05 M Na_2SO_4 and $NaNO_3$ added to the center chamber. The results indicate that these salts do not significantly impact the electrochemical performance of the cell, confirming the robustness of the system under these conditions. Nevertheless, salt accumulation may necessitate periodic removal, which can be achieved through dialysis when employing weak polymeric acids such as polyacrylic acid. Additionally, a small amount of external NaOH may be required to compensate for the net base loss due to SO_x and NO_x neutralization. These findings highlight that while the presence of flue gas contaminants may introduce operational considerations such as pretreatment with a suspension of $CaCO_3$, they do not fundamentally compromise the viability of our approach..

Supplementary Note. S2 | Thermodynamic calculation of the CO_2 absorption and release process.

The reactions happen in absorption process are (K is used to represent equilibrium constant):

$$2NaOH + CO_2 = Na_2CO_3 + H_2O \quad K_1 \tag{S3}$$

$$Na_2CO_3 + CO_2 + H_2O = 2NaHCO_3 \quad K_2 \tag{S4}$$

$$K_1 = \frac{K^{'} \cdot K_{a(H_2CO_3)_1} \cdot K_{a(H_2CO_3)_2}}{K_w^2} = 3.51 \times 10^8 \tag{S5}$$

$$K_2 = \frac{K_{a(H_2CO_3)_1} \cdot K'}{K_{a(H_2CO_3)_2}} = 15.2 \tag{S6}$$

The reactions happen in release process is

$$NaHCO_3 + HOAc = NaOAc + H_2O + CO_2 \quad K_3 \tag{S7}$$

$$Na_2CO_3 + 2HOAc = 2NaOAc + H_2O + CO_2 \quad K_4 \tag{S8}$$

$$K_3 = \frac{K_{a(HOAc)}}{K_{a(H_2CO_3)_1} \cdot K'} = 2.46 \times 10^5 \tag{S9}$$

$$K_4 = \frac{K^2_{a(HOAc)}}{K_{a(H_2CO_3)_1} \cdot K_{a(H_2CO_3)_2} \cdot K'} = 9.23 \times 10^9 \tag{S10}$$

K' is the equilibrium constant of the reaction $H_2O + CO_2 = H_2CO_3$

$[H_2CO_3] = c(CO_{2(aq)}) \cdot K^{'}$. Assuming that the released CO_2 is balanced with CO_2at 1 atm. According to the Henry's Law, $c(CO_{2(aq)})\ (mol/L) = 0.034p(CO_2)(atm)$. The initial concentration c of Na^+ and HOAc is 1.2 M. Assuming that after the reaction was completed, the concentration of the proton is x. [HOAc] can be expressed by x through distribution coefficient as $c \cdot \frac{x}{x + K_{a(HOAc)}}$. $[HCO_3^-]$ can be expressed by x through distribution coefficient as $\frac{c(Carbon) \cdot x \cdot K_{a(H_2CO_3)_1}}{x^2 + x \cdot K_{a(H_2CO_3)_1} + K_{a(H_2CO_3)_1} \cdot K_{a(H_2CO_3)_2}}$, $[CO_3^{2-}]$ can be expressed by x through distribution coefficient as $\frac{c(carbon) \cdot K_{a(H_2CO_3)_1} \cdot K_{a(H_2CO_3)_2}}{x^2 + x \cdot K_{a(H_2CO_3)_1} + K_{a(H_2CO_3)_1} \cdot K_{a(H_2CO_3)_2}}$. $[H_2CO_3]$ can be expressed by x through distribution coefficient as $\frac{c(carbon) \cdot x^2}{x^2 + x \cdot K_{a(H_2CO_3)_1} + K_{a(H_2CO_3)_1} \cdot K_{a(H_2CO_3)_2}}$.

Thus, $\left[HCO_3^-\right]=K^{'}\cdot 0.034p(CO_2)\cdot\frac{x\cdot K_{a(H_2CO_3)_1}}{x^2}$, (S11)

$$\left[CO_3^{2-}\right]=K^{'}\cdot 0.034p(CO_2)\cdot\frac{K_{a(H_2CO_3)_1}\cdot K_{a(H_2CO_3)_2}}{x^2} \quad \text{(S12)}$$

According to the conservation of charge, there is:

$$\left[H^+\right]+\left[Na^+\right]=\left[A^-\right]+\left[OH^-\right]+\left[HCO_3^-\right]+2\left[CO_3^{2-}\right] \quad \text{(S13)}$$

$$x+c=c\cdot\frac{K_{a(HOAc)}}{x+K_{a(HOAc)}}+\frac{K_w}{x}+K^{'}\cdot 0.034p(CO_2)\cdot\frac{x\cdot K_{a(H_2CO_3)_1}+2\cdot K_{a(H_2CO_3)_1}\cdot K_{a(H_2CO_3)_2}}{x^2} \quad \text{(S14)}$$

By solving the equation, we can obtain that $x=1.48\times10^{-8}mol/L$, and $\left[H_2CO_3\right]+\left[HCO_3^-\right]+\left[CO_3^{2-}\right]=1.70\times10^{-3}mol/L$.

This indicates that using acetic acid, its pKa is suitable for the capture and release of CO_2. The theoretical realizing can be >95% of the captured CO_2.

Efficiency:

$$100\%-\frac{\left[H_2CO_3\right]+\left[HCO_3^-\right]+\left[CO_3^{2-}\right]+c(CO_{2(aq)})}{c(C_{initial})}\times100\%$$
$$=100-\frac{1.70\times10^{-3}+0.034}{1.2}\times100\%=97.0\%$$

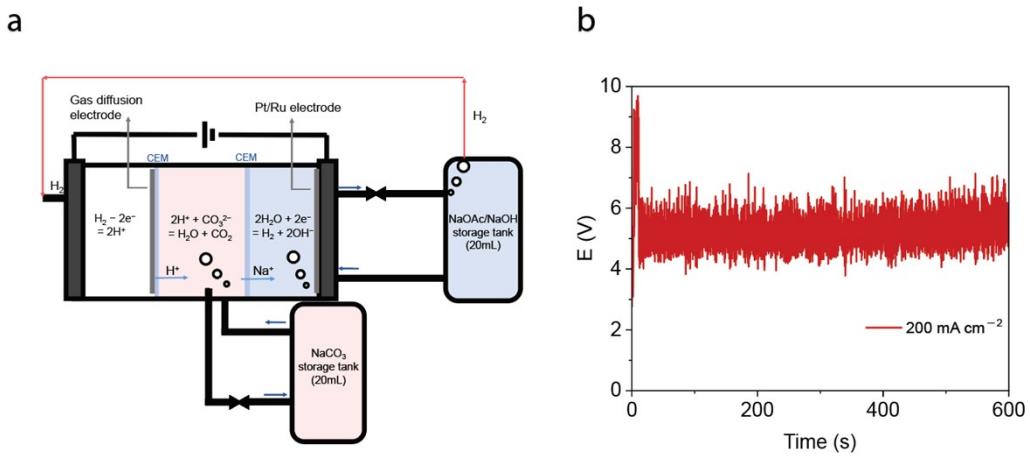

Supplementary Fig. S19 | Electrochemical cell with CO_2 releasing coupled in the cell. a, Schematic of the electrochemical cell. **b,** E-t curve during operation under 200 mA cm^{-2} when directly coupling CO_2 releasing in the cell.

Supplementary Fig. S19a shows that with the supporting electrolyte in the center chamber as Na_2CO_3, bubbles should form in the center. When the generated protons pass through the CEM between anode chamber and center chamber, they will react with carbonate and CO_2 will be released in center chamber. As the CO_2 bubbles keep generating, the ohmic resistance of the electrolyte also fluctuate, leading to the unstable cell voltage shown in Supplementary Fig. S18b. This shows the advantage of generating acid and base while decoupling CO_2 releasing from the cell operation[1, 8].

Supplementary note. S3 | Thermodynamic calculation of the $Ca(OH)_2$ precipitation process.

The reaction happens during the dissolution of $CaCO_3$ is (K is the equilibrium constant):

$$CaCO_3 + 2HOAc = Ca(OAc)_2 + H_2O + CO_2 \qquad K_1 \tag{S15}$$

$$K_1 = \frac{K_{sp(CaCO_3)} \cdot K_{a(HOAc)}^2}{K_{a(H_2CO_3)_1} \cdot K_{a(H_2CO_3)_2} \cdot K'} = \frac{3.36 \times 10^{-9} \times (1.75 \times 10^{-5})^2}{4.2 \times 10^{-7} \times 5.61 \times 10^{-11} \times 1.7 \times 10^{-3}} = 25.7 \tag{S16}$$

K' is the equilibrium constant of the reaction $H_2O + CO_2 = H_2CO_3$

Assuming that the released CO_2 is balanced with CO_2 at 1 atm, and the initial volume V and concentration c of HOAc is 20 mL and 1.2 M. Then we put 1.2 g $CaCO_3$ into the HOAc. Assuming that after the reaction completed, the concentration of the proton is x. The concentration of Ca^{2+} can be expressed as $\frac{K_1 \cdot ([HOAc])^2}{P_{CO_2}/P^{\ominus}}$, and [HOAc] can be expressed by x through distribution coefficient as $c \cdot \frac{x}{x + K_{a(HOAc)}}$. According to the conservation of charge, there is:

$$[H^+] + 2[Ca^{2+}] = [OH^-] + [OAc^-] \tag{S17}$$

$$x + 2\frac{K_1 \cdot (c \cdot \frac{x}{x + K_{a(HOAc)}})^2}{P_{CO_2}/P^{\ominus}} = \frac{K_w}{x} + c \cdot \frac{K_{a(HOAc)}}{x + K_{a(HOAc)}} \tag{S18}$$

By solving the equation, we can obtain that $x = 2.4 \times 10^{-6}$, so the concentration of Ca^{2+} is 0.538 mol L^{-1}. The mass of the dissolved $CaCO_3$ is 1.076 g, thus the efficiency will be 89.7%.

The reaction happen during the production of $Ca(OH)_2$ is:

$$Ca(OAc)_2 + 2NaOH = 2NaOAc + Ca(OH)_2 \qquad K_2 \tag{S19}$$

$$K_2 = \frac{1}{K_{sp(Ca(OH)_2)}} = \frac{1}{5.02 \times 10^{-6}} = 1.99 \times 10^5 \tag{S20}$$

Based on the dissolving process, the initial concentration of $Ca(OAc)_2$ is 0.538 mol L^{-1}, and the volume of the solution is 20 mL. The initial volume V and concentration c of NaOH is 20 mL and 1.2 M. Assuming that after the reaction is completed, the concentration of the proton is x.

The concentration of Ca^{2+} can be expressed as $\frac{x^2}{K_2 \cdot K_w^2}$. According to the conservation of charge, there is:

$$[H^+] + 2[Ca^{2+}] + [Na^+] = [OH^-] + [OAc^-] \quad \text{(S21)}$$

$$x + 2 * \frac{x^2}{K_2 \cdot K_w^2} + 0.6 = \frac{K_w}{x} + 0.538 \times \frac{K_{a(HOAc)}}{x + K_{a(HOAc)}} \quad \text{(S22)}$$

By solving the equation, we can obtain that $x = 1.55 \times 10^{-13}$, so the concentration of Ca^{2+} is 1.21×10^{-3} mol L^{-1}. The theoretical efficiency is 99.8%.

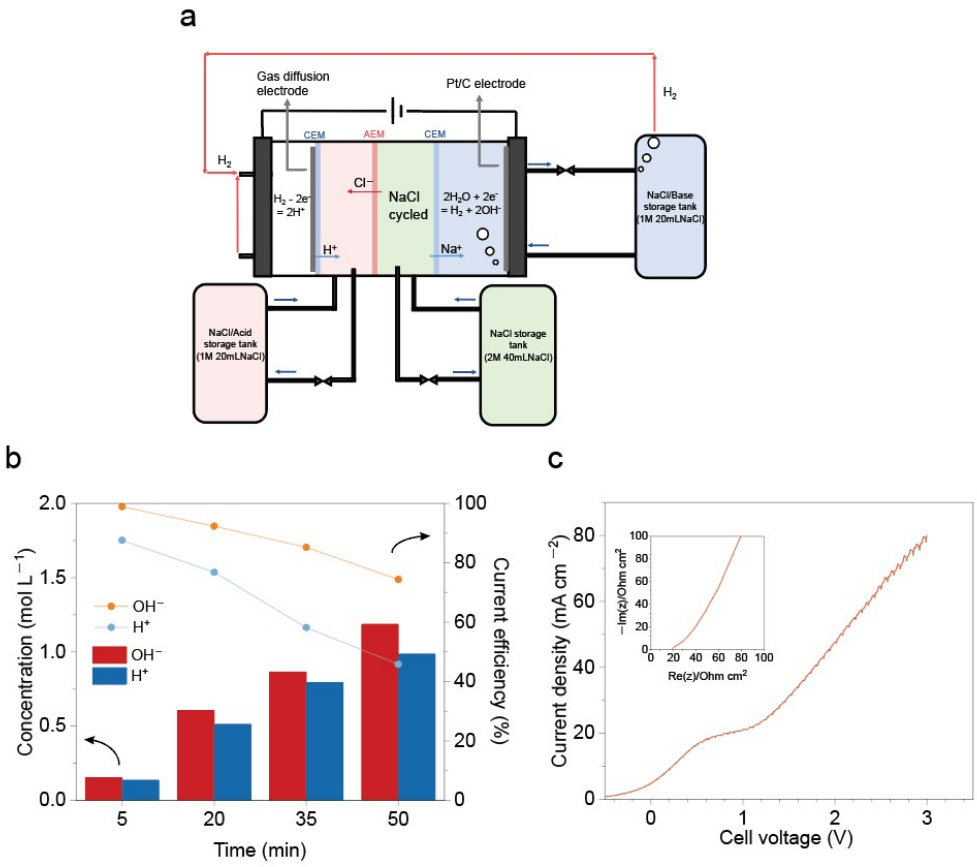

Supplementary Fig. S20 | Four-chamber three membrane acid-base generator, which involves the production of strong acid HCl. a, Schematic of the four-chamber three-membrane acid-base generator**. b,** Differential current efficiency and concentration of generated acid and base during operation. The current density was 200 mA cm^{-2}**. c,** LSV curve and Nyquist plot of a 5 cm^2 acid-base generator with the initial operation condition.

Initially we proposed a four-chamber three-membrane electrochemical cell to generate strong acid and strong base. Supplementary Fig. S20a shows the schematic of the electrochemical cell. The cell consisted of an anode chamber, an acid chamber, a center chamber and a cathode chamber. The acid chamber and anode chamber were separated by one Nafion 212. 20 mL 1 M NaCl was cycled as acid chamber electrolyte, pumped at 53 mL min^{-1}. The acid chamber and center chamber were separated by one DSV-N. 40 mL 2 M NaCl was cycled as center chamber electrolyte, pumped at 53 mL min^{-1}. The center chamber and the cathode chamber were separated by one Fumasep E-610K. 20 mL 1 M NaCl was cycled in the cathode chamber, pumped at 53 mL min^{-1}. The hydrogen oxidation reaction (HOR: $H_2 - 2e^- \rightarrow 2H^+$) and the

hydrogen evolution reaction (HER: $2H_2O + 2e^- \rightarrow H_2 + 2OH^-$) occurred at the anode and cathode, respectively. Hydrogen was introduced into the anode chamber where it undergoes oxidation on a gas diffusion electrode (GDE) to yield protons. These protons traversed the anode CEM while chloride traversed the AEM, so that accumulating acid (HCl) can be collected in the acid chamber. Concurrently, maintaining charge neutrality, sodium ions migrated through the cathode CEM into the cathode chamber, where the hydrogen evolution reaction occurred, leading to the production of sodium hydroxide (NaOH) and enabling the collection of base. The cell was operated with various constant current densities (50 mA cm^{-2}, 75 mA cm^{-2}, 100 mA cm^{-2}, 150 mA cm^{-2}, 200 mA cm^{-2}). When applying a constant current of 200 mA cm^{-2}, the pump and current applied were stopped every 15 minutes. Then we used a pipette to take out 1 mL solution from the solution in acid chamber, solution in center chamber and solution in cathode chamber. Then we used the standard HCl to titrate the solution taken out from cathode chamber, and used the standard NaOH to titrate the solution taken out from acid chamber and center chamber, thus the volume and concentration of the cathode solution at each time point during the operation to take out solution can be determined. By multiplying the volume and concentration, we can obtain the total amount of NaOH or HCl in the corresponding solution, and by subtracting the amount of NaOH or HCl in the solution at two adjacent time points from each other, we can know the increased molarity of NaOH or HCl during these 15 minutes. The theoretical amount of increased molarity NaOH or HCl in 15 minutes can be calculated by integrating the current with time and dividing the result by the Faradaic constant. Finally, by dividing the amount of newly generated NaOH or HCl measured in the experiment by the theoretical amount, we can get the short time current efficiency in every 15 minutes, denoted as differential current efficiency. For current density of 50 mA cm^{-2}, 75 mA cm^{-2}, 100 mA cm^{-2}, 150 mA cm^{-2}, the time period between two operations to take out solution is 60 minutes, 40 minutes, 30 minutes and 20 minutes respectively to ensure that the theoretical amount of newly generated NaOH between two time points under different current densities is the same as the 200 mA cm^{-2} experiment, so that the differential current efficiency is comparable. The integrated current efficiency during the whole experiment can be calculated by integrating differential current efficiency of each short time period. The corresponding integrated energy cost of each accumulated concentrations of acid and base was calculated by integrating cell voltage as a function of capacity passing through the circuit, and multiplying by the integrated current efficiency. Supplementary Fig. S20b shows that the current efficiency of generating NaOH is higher than the current efficiency of generating HCl, indicating that the crossover of proton through AEM is more severe than the crossover of NaOH through CEM.

The polarization of the acid-base generator was analyzed using linear sweep voltammetry (LSV) as shown in Supplementary Fig. S20c. Electrochemical impedance spectroscopy (EIS) was also performed to evaluate the resistance of the cell. The cell demonstrated a current density of about 45 mA cm^{-2} under 2.0 V with a high-frequency area-specific resistance (ASR) of 19 Ω cm^2. The resistance and energy cost is much higher than the three-chamber cell we demonstrated in Fig. 1, due to one extra membrane and one extra center chamber. The current efficiency is low, due to severe proton crossover when using strong acid.

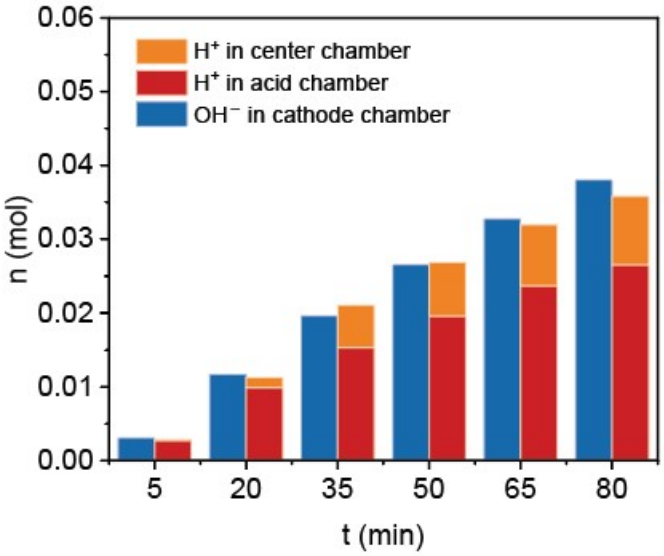

Supplementary Fig. S21 | A comparison of the amount of hydroxide in cathode chamber and the sum of the amount of proton in center chamber and acid chamber.

Fast crossover of protons also causes the trouble of efficiently collecting acids. We calculated the amount of NaOH in cathode chamber and the amount of HCl in acid chamber and center chamber at each time point. By comparing the amount of hydroxide in cathode chamber and the sum of the amount of proton in center chamber and acid chamber, we found that those two numbers were almost the same. The result shows that the difference in current efficiency was solely caused by the severity of proton crossover.

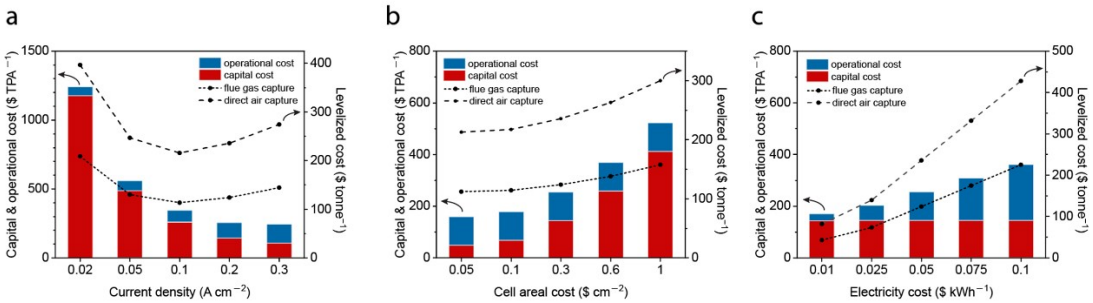

Supplementary Fig. S22 | Techno-economic analysis (TEA). The operational cost, capital cost, and levelized cost of acid-base generator at different **a,** current densities, **b,** cell areal costs and **c,** electricity costs. The default value of current density, cell areal cost, and electricity cost were set to be 0.2 A cm^{-2}, 0.3 $ cm^{-2}, 0.05 $ kWh^{-1}, respectively. In each plot, only one parameter was set as the variable; other parameters were set as constants.

In this section, we further study the capital cost, operational cost and levelized cost of captured carbon using the multi-chamber electrochemical cell. These costs depend on the cost of several components of the electrochemical cell. The capital cost of acid-base generator is strongly correlated to the current density and the areal cost of the cell, whereas the operational cost is mainly subject to the cost of electricity.

As shown in Supplementary Fig. S22a, with higher current density, the capital cost decreases due to smaller electrochemical cells required. But operational cost increases due to higher voltage used to drive the reaction. As a result, the levelized cost decreases then increases with a higher current density.

As shown in Supplementary Fig. S22b, higher areal cost of electrochemical cells will increase the capital cost. Supplementary Fig. S22c shows that higher cost of electricity will increase the operational cost and significantly increase the levelized cost of carbon dioxide. Cheap, green electricity is crucial to make the acid-base generation system commercially attractive.

The detailed techno-economic analysis is shown as follows.

Input values for economic analyses of an acid-base generator for carbon capture are as follows for a 10 year project:

M is the molecular weight of carbon dioxide in g mol^{-1}, equaling 44.

F is the Faradaic constant in C mol^{-1}, equaling 96485.

n is the number of electrons transferred during production of sodium hydroxide for CO_2 capture, equaling 1.

t is the time of a year in s, equaling 365*24*3600.

m is the mass of produced CO_2 per year (counted as pure) in grams, equaling 1000000 when producing 1 tonne per year.

η is the overall current efficiency in capturing carbon dioxide using sodium hydroxide. We assume η = 0.5 for direct air capture (about 2 hydroxide ions capturing one carbon dioxide) and η = 0.95 for flue gas capture (about 1 hydroxide ions capturing one carbon dioxide).

I is the current density of the cell in A cm^{-2}, with a default value assumed as 0.2.

V is the voltage of the cell in V. Fitted from experiments, we use $V = 1.0 + 7.8 * I$.

$Cost_{cell\ areal}$ is the areal cost of the cell in \$ cm^{-2}, with a default value assumed as 0.3.[1]

Area is the area of the cell for the production of 1 tonne (1000000 g) CO_2 per annual (TPA) in cm^2, where $Area = \frac{m * n * F}{M * I * t}$.

$Cost_{cell}$ is the capital cost of the electrochemical cell in \$ TPA^{-1}, where $Cost_{cell} = Cost_{cell\ areal} * Area$.

$Cost_{other}$ is the capital cost of other equipment and electrolyte in \$ TPA^{-1}, assumed as 30.[14, 15]

$Cost_{capital}$ is the capital cost of the whole system in \$ TPA^{-1}, where $Cost_{capital} = (Cost_{cell} + Cost_{other}) * \eta^{-1}$.

$Cost_{electricity}$ is the cost of electricity in \$ kWh^{-1}, with a default value assumed as 0.05.

$Cost_e$ is the cost of electricity during the system operation in \$ TPA^{-1}, where $Cost_e = \frac{m * n * F * V * Cost_{electricity}}{M * 1000 * 3600}$.

$Cost_{otheropex}$ is the operational cost of other maintenance and electrolyte in \$ TPA^{-1}, assumed as $5 + 400 * Cost_{electricity}$.

$Cost_{opex}$ is the operational cost of the whole system during operation in \$ TPA^{-1}, where $Cost_{opex} = (Cost_e + Cost_{otheropex}) * \eta^{-1}$.

Capital cost is assumed to happen in and only in the first year, without production of any product. Operational costs happen every following year, producing 1 tonne carbon dioxide annually.

r is the annual discount rate, whose value is set as 0.05, for a ten-year project.

$Cost_{CO2}$ is the levelized cost of produced CO_2, in \$ $tonne^{-1}$.

***NPV* is the cumulative net product value of the produced carbon dioxide.**

$$NPV = -Cost_{capital} + \sum_{year=2}^{year=10} (Cost_{CO2} - Cost_{opex})(1-r)^{year}$$

$Cost_{CO2}$ is resolved by setting $NPV = 0$.

The economic viability of CO_2 capture technologies is determined by both capital and operational costs. Traditional amine-based and porous material-based capture methods require continuous replenishment of sorbents and suffer from degradation issues, leading to high operational expenses. In contrast, our electrochemical approach offers a fundamentally different cost structure.

The capital cost of our system is dominated by the electrochemical cell, but this cost is independent of the total CO_2 capture capacity. Additionally, the operational cost is primarily dictated by electricity consumption, which can be minimized through process optimization and the use of renewable energy sources. The technoeconomic tradeoff of *1:* large cell area/low current density, which saves overvoltage and energy cost; *vs. 2:* small cell area/high current density, which saves capital cost; needs be settled in future work.

Moreover, our method enables applications such as direct air capture (DAC) and green slaked lime production, which are challenging to achieve with amine-based methods. The ability to electrochemically generate alkaline capture agents potentially reduces material handling and disposal costs, further enhancing economic feasibility. At large scales, these advantages position electrochemical CO_2 capture as a potentially competitive alternative to conventional methods, particularly in scenarios where flexible and modular deployment is desired.

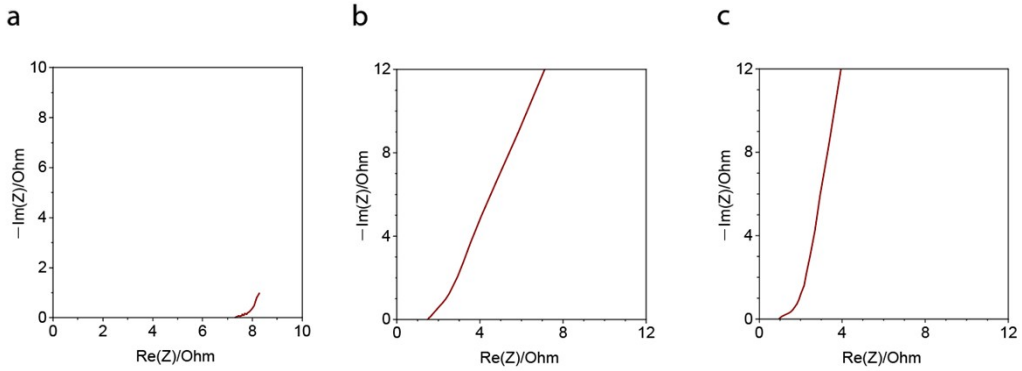

Supplementary Fig. S23 | Nyquist plot of other prototype cells. a, Nyquist plot of the BPM based four-chamber three-membrane acid-base generator driven by non-PCET reversible redox reactions. **b,** Nyquist plot of the three-chamber two-membrane acid-base generator driven by OER and ORR**; c,** Nyquist plot of the acid-base generator driven by water splitting

As Supplementary Fig. S23 shows, the high frequency resistance of the cell significantly decreases as the number of chambers and membranes in the cell decrease.

a

b

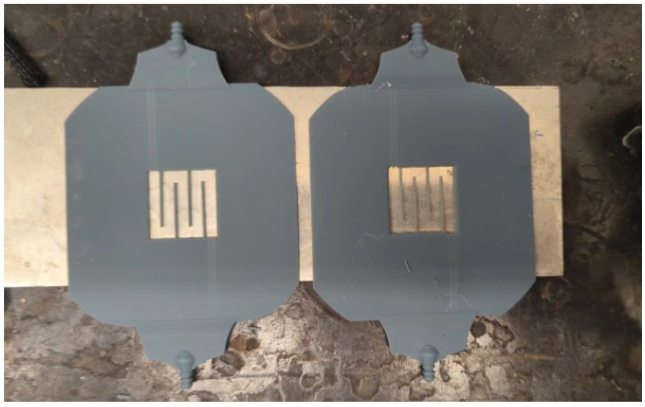

Supplementary Fig. S24 | Process of making center chambers with flow fields by 3-D printing. a, Initially printed center chambers. **b,** Final image of the center chamber. Flow field is created by cutting off part of the sticks in the window.

1. Zhu, P.; Wu, Z.-Y.; Elgazzar, A.; Dong, C.; Wi, T.-U.; Chen, F.-Y.; Xia, Y.; Feng, Y.; Shakouri, M.; Kim, J. Y.; Fang, Z.; Hatton, T. A.; Wang, H., Continuous carbon capture in an electrochemical solid-electrolyte reactor. *Nature* **2023,** *618* (7967), 959-966.
2. Zhang, X.; Fang, Z.; Zhu, P.; Xia, Y.; Wang, H., Electrochemical regeneration of high-purity CO2 from (bi) carbonates in a porous solid electrolyte reactor for efficient carbon capture. *Nat. Energy* **2024**, 1-11.
3. Davis, S. M.; Gray, G. E.; Kohl, P. A., Candidate membranes for the electrochemical salt-splitting of Sodium Sulfate. *J. Appl. Electrochem.* **2008,** *38*, 777-783.
4. Tzanetakis, N.; Varcoe, J.; Slade, R.; Scott, K., Salt splitting with radiation grafted PVDF anion-exchange membrane. *Electrochem. Commun.* **2003,** *5* (2), 115-119.
5. Xu, Y.; Liu, S.; Edwards, J. P.; Xiao, Y. C.; Zhao, Y.; Miao, R. K.; Fan, M.; Chen, Y.; Huang, J. E.; Sargent, E. H.; Sinton, D., Regeneration of direct air CO2 capture liquid via alternating electrocatalysis. *Joule* **2023,** *7* (9), 2107-2117.
6. Digdaya, I. A.; Sullivan, I.; Lin, M.; Han, L.; Cheng, W.-H.; Atwater, H. A.; Xiang, C., A direct coupled electrochemical system for capture and conversion of CO2 from oceanwater. *Nat. Commun.* **2020,** *11* (1), 4412.
7. Gilliam, R. J.; Boggs, B. K.; Decker, V.; Kostowskyj, M. A.; Gorer, S.; Albrecht, T. A.; Way, J. D.; Kirk, D. W.; Bard, A. J., Low voltage electrochemical process for direct carbon dioxide sequestration. *J. Electrochem. Soc.* **2012,** *159* (5), B627.
8. Yan, L.; Bao, J.; Shao, Y.; Wang, W., An electrochemical hydrogen-looping system for low-cost CO2 capture from seawater. *ACS Energy Lett.* **2022,** *7* (6), 1947-1952.
9. Schiffer, Z. J.; Lucas, É.; Watkins, N. B.; Ardo, S.; Xiang, C.; Atwater, H. A., Acid and base generation via an electrochemical hydrogen-looping cell tailored for carbon removal applications. *Device* **2024**.
10. Ellis, L. D.; Badel, A. F.; Chiang, M. L.; Park, R. J.-Y.; Chiang, Y.-M., Toward electrochemical synthesis of cement—An electrolyzer-based process for decarbonating CaCO3 while producing useful gas streams. *Proceedings of the National Academy of Sciences* **2020,** *117* (23), 12584-12591.
11. Guan, X.; Zhang, G.; Li, J.; Kim, S. C.; Feng, G.; Li, Y.; Cui, T.; Brest, A.; Cui, Y., Seawater alkalization via an energy-efficient electrochemical process for CO2 capture. *Proceedings of the National Academy of Sciences* **2024,** *121* (45), e2410841121.
12. Zhao, D.; Zhuang, Z.; Cao, X.; Zhang, C.; Peng, Q.; Chen, C.; Li, Y., Atomic site electrocatalysts for water splitting, oxygen reduction and selective oxidation. *Chem. Soc. Rev.* **2020,** *49* (7), 2215-2264.
13. Xi, D.; Yang, Z.; Alfaraidi, A. M.; Jing, Y.; Gordon, R. G.; Aziz, M. J., Single-membrane pH-decoupling aqueous batteries using proton-coupled electrochemistry for pH recovery. *Energy Advances* **2024**.
14. Darling, R. M.; Gallagher, K. G.; Kowalski, J. A.; Ha, S.; Brushett, F. R., Pathways to low-cost electrochemical energy storage: a comparison of aqueous and nonaqueous flow batteries. *Energy Environ. Sci.* **2014,** *7* (11), 3459-3477.
15. Keith, D. W.; Holmes, G.; Angelo, D. S.; Heidel, K., A process for capturing CO2 from the atmosphere. *Joule* **2018,** *2* (8), 1573-1594.